Efficient Perovskite Solar Cells by Metal Ion Doping

AUTHOR INFORMATION

Jacob Tse-Wei Wang,[1] Zhiping Wang,[1] Sandeep Pathak,[1] Wei Zhang, [‡1] Dane W. deQuilettes,[2]

Florencia Wisnivesky,[3] Jian Huang,[1] Pabitra Nayak,[1] Jay Patel,[1] Hanis Yusof,[4] Yana Vaynzof,[5,6]

Rui Zhu,[7] Ivan Ramirez,[1] Jin Zhang,[1] Caterina Ducati,[3] Chris Grovenor,[4] Michael B. Johnston, [1]

David S. Ginger,[2] Robin J. Nicholas[1]* & Henry J. Snaith[1]*

[1]Department of Physics, University of Oxford, Clarendon Laboratory, Parks Road, Oxford OX1 3PU, UK

[2]Department of Chemistry, University of Washington, Box 351700, Seattle, WA 98195-1700, USA

[3]Department of Materials Science and Metallurgy, University of Cambridge, 27 Charles Babbage Road, Cambridge CB3 0FS, United Kingdom.

[4]Department of Materials, University of Oxford, Parks Road, Oxford, OX1 3PH, UK

[5]Kirchhoff Institute for Physics (KIP), Im Neuenheimer Feld 227, 69120 Heidelberg, Germany

[6]Centre for Advanced Materials (CAM), Im Neuenheimer Feld 225, 69120 Heidelberg, Germany

[7]State Key Laboratory for Artificial Microstructure and Mesoscopic Physics, School of Physics, Peking University, Beijing, China, 100871

‡ Current address: School of Chemistry, Joseph Banks Laboratories, University of Lincoln, Beevor Street, Lincoln LN6 7DL, UK.

Corresponding Author

*r.nicholas1@physics.ox.ac.uk; *henry.snaith@physics.ox.ac.uk

BROADER CONTEXT

Perovskite solar cells, which promise to deliver the highest efficiency, lowest cost next-generation PV technology, have been largely advanced over the last few years by improvements in the polycrystalline thin film quality. So far, improvements in film uniformity and smoothness, have mainly been at the expense of crystalline grain-size, and charge recombination losses at defect sites. High luminescence efficiency, which is an indication of better optoelectronic quality, has generally been found in films with polycrystalline grains of many micrometres in scale. This suggests a current compromise between ideal morphology and ideal optoelectronic quality.

For traditional semiconductors and crystalline solids, the influence of impurity ion doping has been studied extensively and can either alter the crystallisation or induced electronic positive or negative type doping. However, in the perovskite community, impurity doping has been largely unexplored. Here, we show that doping the perovskite solution with Al^{3+}, which has a much smaller ionic radius than Pb^{2+}, has profoundly positive influenced on the crystalline and optoelectronic quality of the perovskite absorber layer: We demonstrate a two-fold increase in the photoluminescence quantum efficiency and a significantly reduced electronic disorder, despite the films still having polycrystalline grains on the order of one micrometer is scale. This largely overcomes the trade-off between film smoothness and optoelectronic quality, and these improvements translate into highly efficient planar heterojunction perovskite solar cells.

Our work paves the way for further improvement of the optoelectronic quality of perovskite thin films, and subsequent devices, via highlighting a new avenue for investigation of the role of dopant impurities upon crystallisation and controlling the electronic defect density in the perovskite thin films.

ABSTRACT

Realizing the theoretical limiting power conversion efficiency (PCE) in perovskite solar cells requires a better understanding and control over the fundamental loss processes occurring in the bulk of the perovskite layer and at the internal semiconductor interfaces in devices. One of the main challenges is to eliminate the presence of charge recombination centres throughout the film which have been observed to be most densely located at regions near the grain boundaries. Here, we introduce aluminium acetylacetonate to the perovskite precursor solution, which improves the crystal quality by reducing the microstrain in the polycrystalline film. At the same time, we achieve a reduction in the non-radiative recombination rate, a remarkable improvement in the photoluminescence quantum efficiency (PLQE) and a reduction in the electronic disorder deduced from an Urbach energy of only 12.6 meV in complete devices. As a result, we demonstrate a power-conversion efficiency (PCE) of 19.1% with negligible hysteresis in planar heterojunction solar cells comprising all organic p and n-type charge collection layers. Our work shows that an additional level of control of perovskite thin film quality is possible via impurity cation doping, and further demonstrates the continuing importance of improving the electronic quality of the perovskite absorber and the nature of the heterojunctions to further improve the solar cell performance.

INTRODUCTION

Driven by improvements in the quality of organic-inorganic lead halide perovskites (i.e. $CH_3NH_3PbI_3$) thin films, perovskite solar cells have achieved a series of efficiency breakthroughs since 2009.[1-4] Starting from structures based on small nanocrystals embellishing the surface of a

4

mesoporous TiO_2 scaffold in 2009, the published highest power conversion efficiency of 21.1% has been achieved in a device architecture which comprises both a thin layer of mesoporous TiO_2 and a thick solid perovskite absorber layer with micrometre size crystalline domains and a high level of uniformity.[5] In addition, there has been much work on the simplified "planar heterojunction" architecture, where a solid perovskite absorber layer is sandwiched between negative (n) and positive (p) type charge collection layers.[2,6] One commonality of all this work, is that enhanced crystalline quality and the macroscopic uniformity of the solid perovskite thin films are key parameters which have led to improved device performance. However, there is still much confusion over many factors such as the role and impact of boundaries between the polycrystalline domains, the requirement or not to move towards single crystalline materials, the nature and role of electronic defects in the perovskite absorbers, and the impact of the charge collection layers upon loss processes in the perovskite solar cells.

One specific area which has had some attention is the precise nature of electronic defects in the perovskite films. Yan et al. have used theoretical calculations to propose that many of the defects, such as I or Pb vacancies, will result in states very close to or within the continuum of states in the conduction and valance bands; therefore only having a minor negative electronic impact upon the solar cells.[7] However, Agiorgousis et al. have revealed that there is strong covalency between the Pb cations and I anions in the perovskite plane, which may result in the existence of intrinsic defects, such as undercoordinated Pb dimers and I trimers, which could generate sites within the band gap and serve as charge recombination centres during solar cell operation.[8]

Previously, post treatment of the perovskite films with Lewis bases, such as pyridine, has been shown to enhance the charge carrier lifetime,[9] suggesting that pyridine can passivate the

surface recombination sites,[9] which are possibly under-coordinated Pb sites.[10] However, these sorts of post growth treatments are challenging to control in a reproducible manner, and it is not clear if they are genuinely passivating the defect sites, or simply enabling the perovskite crystal surface to reconstruct in a more favorable manner with fewer crystal surface defects.[9] On the other hand, incorporation of an impurity "dopant" into the precursor solution itself could provide a more robust way to produce a perovskite film with traps passivated throughout the bulk, or indeed influence the crystallization process in such a way as to minimize the number of defects which result in electronic traps in the first place.[11] Recently, Sargent and coworkers have shown that addition of Phenyl-C_{61}-butyric acid methyl ester (PCBM) directly into the perovskite precursor solution allows PCBM to sit at the grain boundaries of the processed perovskite films, leading to a certain degree of passivation of the trap states at the grain boundaries, and suppression of hysteresis in the n-i-p planar heterojunction device architecture.[12] In addition, PCBM is a very good electron acceptor for use as the n-type charge collection material in perovskite solar cells, hence its role may be two-fold when mixed into the perovskite solution.[13] However, a major challenge to achieving reproducible device performance with this route is the poor solubility and significant phase segregation of PCBM within the perovskite precursor solution.[12]

Here, we investigate the impact of "doping" the perovskite, $CH_3NH_3PbI_3$ ($MAPbI_3$), with Al^{3+}, a higher valence metal ion than Pb^{2+}. We introduced a Lewis acid-base coordination complex, aluminium acetylacetonate (Al-$acac_3$), directly into the perovskite precursor solution, which contains Pb acetate trihydrate ($PbAc_2.(3H_2O)$) and methyl ammonium iodide (MAI).[14] Al^{3+} ions have a much smaller ionic radii than Pb^{2+} (53.5 pm vs 119 pm) hence we do not expect to observe substitutional doping within the crystal.[15] However, by careful optimization of the Al^{3+}

ion concentration in the perovskite precursor solution, we dramatically enhance the PLQE of the crystalized perovskite films, which increases to 35 % from only 15 % for the non-doped (control) films when measured at ~ 10 suns irradiance, which we infer to be due to a reduction in the density of electronic defects. By incorporating these "Al^{3+}-doped" films into "inverted" p-i-n perovskite solar cells, we achieve a measured current-density voltage PCE of 19.1% and a stabilized power output of 18.2%.

RESULTS AND DISCUSSION

To deposit Al^{3+}-doped $MAPbI_3$ perovskite films, we first prepared a $MAPbI_3$ precursor solution by mixing MAI and $PbAc_2.(3H_2O)$ at a 3:1 molar ratio in dimethylformamide (DMF), with the addition of hypophosphorous acid, as previously reported by Zhang et al.[11] In order to study the impact of doping concentration on the perovskite, we added varying concentrations (from 0.075 to 1.5 mol% of the Al^{3+}/Pb^{2+} ratio) of Al-$acac_3$ into the as prepared $MAPbI_3$ precursor solutions and fabricated a series of perovskite films. We note that, in this manuscript we will refer to the Al-$acac_3$ addition as "Al^{3+} doping". We will show evidence towards the end of the manuscript that it is indeed the addition of aluminum ions, and not the organic counter ions which is important for the improvements which we will present. We first evaluate if there is any impact of Al^{3+} doping upon the crystallization process and the final crystal structure of the resulting perovskite films. In fig. 1a and fig. S1 we show the X-ray diffraction (XRD) spectra for a series of films made with a range of Al^{3+} doping concentrations up to 1.5 mol%. All the perovskite films crystallise in a typical tetragonal crystal (*I4/mcm, NO. 140*) structure as reported previously.[1] As the doping levels increase up to 0.15 mol%, the intensities of the dominant perovskite (110) and (220) peaks substantially increase with increasing doping concentration,

and there is a significant decrease in peak widths (see fig. S2) but no measurable shift in the position of the (110) and (220) diffraction peaks. These results suggest that the (hh0) planes become increasingly aligned in the presence of the Al^{3+} dopant. As the doping level rises to 0.3 mol% concentration, the (110) peak intensity continues to increase, but the peak begins to broaden and shift in position with respect to the control sample. However, upon further increase in doping concentration, the peak intensity begins to decrease and the peak widths continue to broaden.
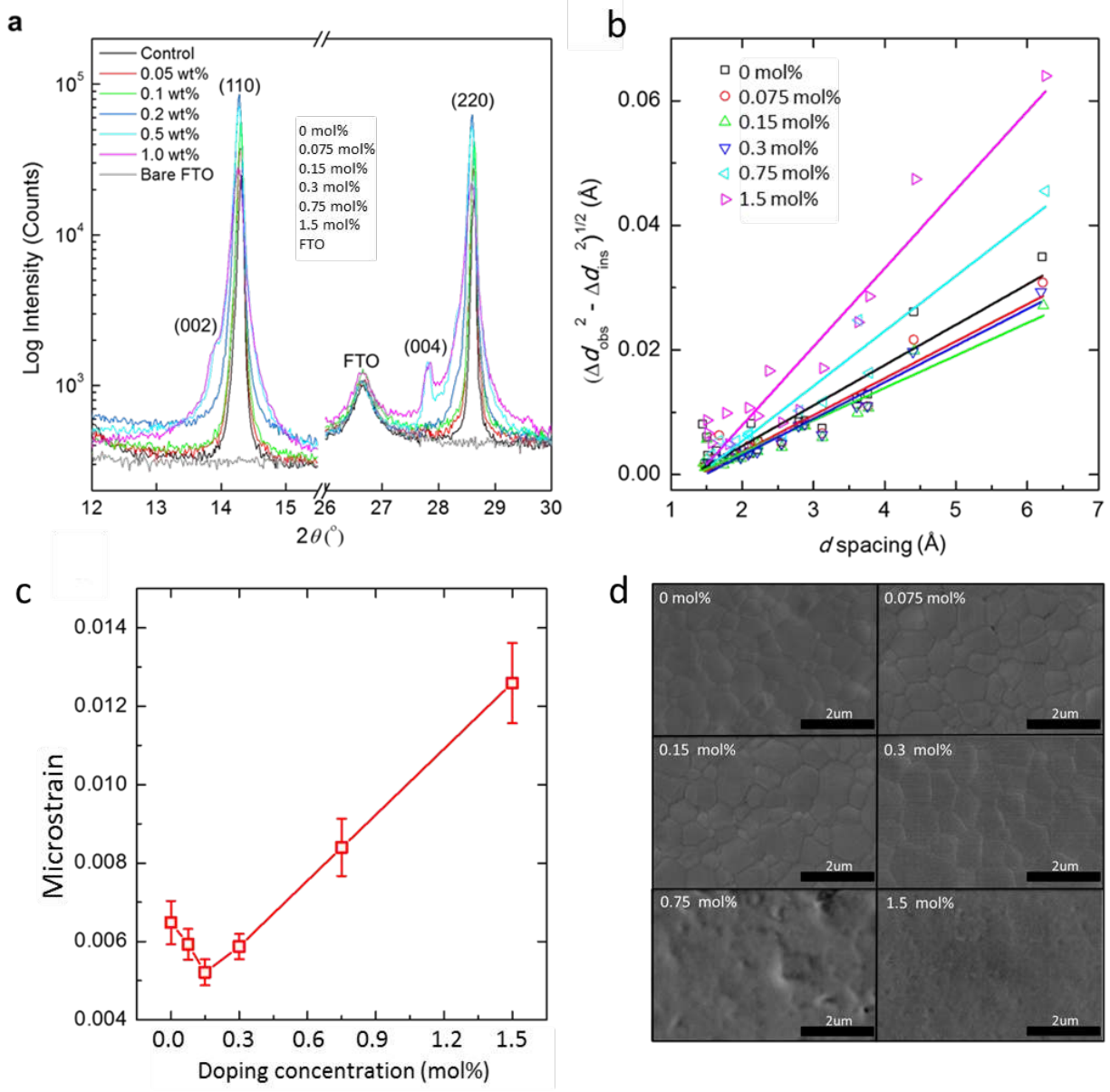
Figure 1. Characterizations of control and Al^{3+}-doped perovskite samples with **(a)** X-ray diffraction patterns analysis, and **(b)** A modified Williamson-Hall plot of $(\Delta d_{obs}^2 - \Delta d_{ins}^2)^{1/2}$ versus d spacing extracted from the corresponding diffraction profiles shown in Fig. S1. The slopes of the solid lines from linear fits indicate the extents of microstrain at different doping concentrations. **(c)** Calculated microstrain of samples with different Al^{3+} doping concentration

from XRD patterns (The error bars for each concentration in the plot c, are determined from the fits in b). **(d)** top view scanning electron microscope (SEM).

Broadening and shifts in the XRD peak can be caused by either a reduction in the grain size (Scherrer broadening) and/or non-uniform strain (microstrain). We note that Scherrer broadening will only be significant when the grains are in the range of or less than 100nm, and as we will discuss later we do not expect this to be a significant contribution here. Strain is the relative change in size of an object with respect to its ideal size (or size before experiencing an external force). The microstrain in a crystalline material is a result of small fluctuations in the lattice spacing, induced by crystal imperfections/structural defects including dislocations, vacancies, stacking faults, interstitials, twinning, and grain boundaries.[16,17,18] By simply considering Braggs law for scattering of light of wavelength λ, $n\lambda = 2d\sin\theta$, it is clear that small fluctuations in d (i.e. Δd) will result in small fluctuations, or broadening, in θ when measuring the X-ray diffraction from the material. We quantify the extent of microstrain in our perovskite films by analysing the peak broadening in the diffraction patterns according to the modified Williamson-Hall method.[17,19] The effective observed d-space broadening (Δd_{obs}) determined from the XRD peak width broadening, is a convoluted function of the Gaussian full width half maximum broadening in the 2θ scan due to the instrument response (Δd_{ins}), the grain size (Δd_{size}) and the microstrain (Δd_{ε}). These can be de-convoluted from the observed broadening, via,

$$\Delta d^2_{obs} = \Delta d^2_{\varepsilon} + \Delta d^2_{ins} + \Delta d^2_{size} \tag{1}$$

where the unit-less microstrain ε is defined as $\varepsilon = (\Delta d_{\varepsilon}/d)$, where d is the mean d-spacing.

Since the perovskite thin films have grains on the order of many hundreds of nm to microns, it is likely that the size effect induced peak width broadening can be neglected, hence if $\Delta d^2_{size} << \Delta d^2_{obs}$ [19] and we can write,

$$(\Delta d^2_{obs} - \Delta d^2_{ins})^{1/2} \approx \varepsilon d. \qquad (2)$$

Therefore, the slope of $(\Delta d^2_{obs} - \Delta d^2_{ins})^{1/2}$ versus d, gives the magnitude of the microstrain, ε, in the film.

Here we observe in figure 1b and c that introduction of small amounts of Al^{3+} dopant (< 0.3 mol%) decreases the microstrain. A minimum microstrain of 5.2×10^{-3} is achieved at 0.15 mol%, which is 30% lower than the control film. We note that this is equivalent to d-spacing fluctuations of the order of 0.5%. This suggests that the introduction of a small amount of Al^{3+} dopant reduces the density of crystal defects. Additionally, the (110) XRD peak significantly increases in intensity, consistent with the presence of Al^{3+} enhancing the orientation in the growth of perovskite domains along the (110) plane.[20]

If the Al^{3+} ions partially substitute Pb^{2+} ion sites, we would expect the perovskite lattice to be severely distorted due to the much smaller Al^{3+} ionic radii as compared to the Pb^{2+} ion, which would induce a shift in d.[21] Following this reasoning, the unvarying (hh0) peak position and decreased microstrain imply at the doping level of 0.15%, the Al^{3+} dopants are unlikely to be incorporated within the perovskite crystal lattice. When the doping concentration increases to 0.3 mol%, we observe an increase in microstrain, which continues to increase monotonically with the increasing doping concentration.

In fig. 1d we show top-view SEM images of the perovskite samples with different doping concentrations of Al^{3+}. We do not observe any noticeable differences in morphology or apparent grain size in the perovskite films up to doping levels of 0.3 mol%, compared to the control

sample. This is consistent with our postulation that the narrowing of the (hh0) diffraction peaks with the doping concentration from zero to 0.15 mol% is not due to crystal size effects. Morphologically, it appears that the perovskite films can tolerate the addition of Al^{3+} ions to the precursor solution up to around 0.3 mol%, before any negative impact upon the morphology occurs. The disappearance of the polycrystalline grains in the SEM images, with Al^{3+}concentrations at or above 0.75 mol%, is consistent with these films having much smaller polycrystalline domains, which are not clearly discernible in the SEM image. We also note that the XRD patterns for the films with over 0.3 mol% doping, which we have shown in Fig. 1a, are strongly perturbed, indicating a limit to the concentration of Al^{3+} which the perovskite films can tolerate.

To probe whether Al ions remain in the annealed films, we performed inductively coupled plasma optical emission spectrometry (ICP-OES). The detection limits of ICP-OES typically range from parts per million (ppm) to parts per billion (ppb).[22] For the sample with 0.15 mol% Al^{3+} doping (the calculated Al/Pb is 2.6:1000), we determine a molar ratio of Al/Pb of 1.2:1000 from the ICP-OES analysis, which confirms the presence of Al^{3+} in the doped film, only at a slightly lower concentration than in the starting solution. On the contrary, for the control film we determine an Al/Pb molar ratio of 0.016:1000, which is almost negligible, as expected. We further validated this finding for higher concentration solutions (>0.3 mol%) using X-ray photoelectron spectroscopy (see fig. S3).

To further investigate the location and distribution of the Al^{3+} ions within the perovskite film, we employed nanoscale secondary ion mass spectrometry (NanoSIMS) to perform elemental mapping for the doping level of 0.15 mol%. The NanoSIMS system uses a 16 KeV

primary $^{133}Cs^+$ beam to bombard the perovskite film surface, and then collects and analyzes the Al signal as a negative ion which is commonly detected as AlO^- (the oxygen is captured from the sample surface or the vacuum system). In fig. S4 we show the secondary electron SEM images overlaid with the elemental map for Al. In the secondary electron image the darker regions are regions of thicker films, which we therefore interpret as being the centre of grains, and the lighter regions are the thinner regions which we therefore interpret to be the grain boundaries. Although the Al signal is apparent everywhere in the film, it is most strongly concentrated near the brighter regions of the secondary electron microscopy image, indicative of increased Al concentration near the grain boundaries. This is consistent with the Al^{3+} ions being predominantly expelled to the perovskite surface and grain boundaries during crystallisation.

Considering all the evidence we have presented above, it appears that the presence of a small amount of Al^{3+} in the perovskite growth solution results in better crystallisation with resultantly fewer crystal defects, as we infer from the reduced microstrain. However, beyond an optimum level of addition of Al^{3+}, the crystallization is strongly perturbed resulting in increased levels of defects. At low Al^{3+} doping concentrations, the Al^{3+} ions appear not to be incorporated into the perovskite lattice, but predominantly expelled to the surface and grain boundaries. The precise mechanism by which the crystallisation is enhanced with a small quantity of Al^{3+} doping is difficult to determine. However, based on our investigation above, we describe our postulated mechanism here: The presence of impurity ions is known to influence crystallisation of materials since the earliest investigations of crystal growth.[23] Impurity ions can either slow down crystallisation by adsorbing to crystal surfaces and sterically inhibiting growth, or the impurity ions can accelerate crystal growth by changing the surface energy of the crystal growth front making it more favourable for accelerated crystallization.[24–26] In the low concentration regime

(below 0.3mol% Al^{3+}) we infer that the Al^{3+} is facilitating enhanced crystallization, and specifically the growth of (*hh0*) crystal planes, resulting in more orientated crystalline domains. In fig. 2, we show a schematic diagram of the proposed perovskite growth mode and influence of the Al^{3+} doping. We also illustrate crystal defects which could potentially exist at the edges of the perovskite crystal surface in the form of terraces, and indicate how the Al^{3+} doping can reduce the prevalence via the selective enhancement of growth of these terraces.

In order to visualize how the Al^{3+} doping has influenced the as-crystalized films, we performed atomic force microscopy (AFM) measurements on our samples. We show these images in Figure 2, and plot histograms for the distribution in heights from the images. The lower regions correspond to the troughs at the boundary of the grains, and the higher regions correspond to the top most surfaces of the grains. For the control sample we observe a symmetric, approximately Gaussian distribution of heights, indicating that the surface of the perovskite film is continuously undulating over the measured length-scale, with no specific preferred height. We estimate a half-width at half-maximum (HWHM) height distribution of ~33 nm. This level of undulation is almost identical to the underlying FTO substrate, which we determine a HWHM height distribution of 34 nm, which we show in the SI. Thus the control perovskite film does not appear to planarize the FTO. In contrast for the optimum (0.15 mol%) doped perovskite sample, the height distribution becomes asymmetric with a background undulation of the same extent, but with an additional distribution with a much narrower HWHM of ~16 nm on the top-most region of the films. This indicates that the top of the grains are much flatter in the Al^{3+} doped samples than in the control samples. The height distribution for the 1.5% Al^{3+} doped sample significantly changes, but still shows a relatively narrow distribution on the top surface and a long tail indicating a relatively flat film, but now with the presence of pinholes.

Since the crystal morphology of the 1.5% sample has changed considerably, we can-not compare this directly to the other two compositions. These observations further corroborate that, with low levels of Al^{3+} doping, the perovskite crystalline growth is indeed enhanced and preferentially selects certain planes, while in addition the reduced roughness of the surface of the grains is consistent with a reduction in terrace/step-like defects on the crystal surface.
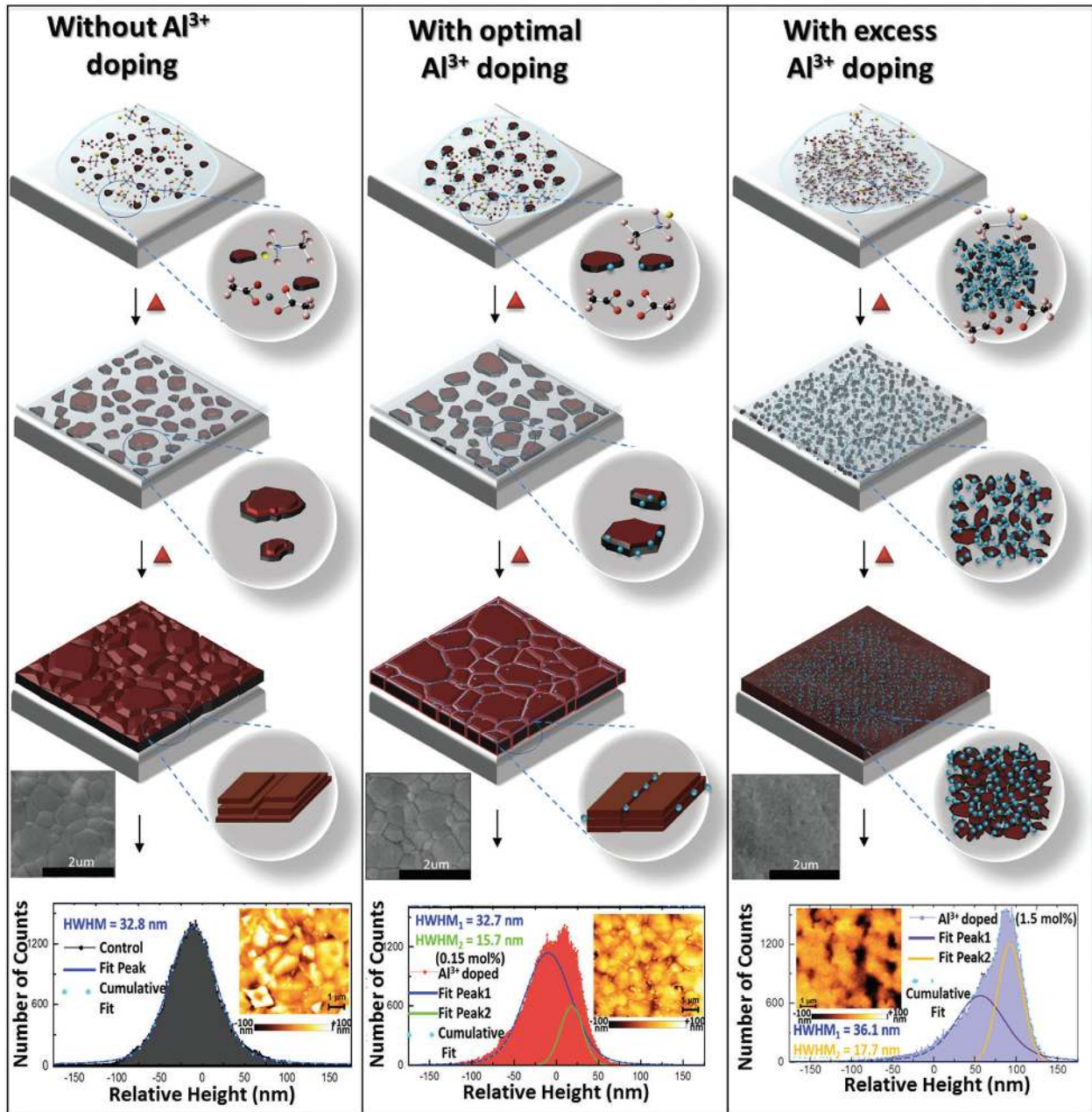
Figure 2: Schematic diagram of the proposed perovskite polycrystalline thin film growth and influence of the Al^{3+} doping with illustrated C, N, H, O, I, Pb, and Al atoms are indicated by the color of black, blue, pink, red, grey, and cyan respectively; And histograms of the surface topography and the images (insets) from AFM measurements of different samples. Best fits for the histograms are obtained using one and two Voigt distributions, respectively for the control and the optimized sample. The individual distribution components with their HWHM, and the cumulative fits are labelled as in the figure.

We now investigate if the structural improvements in the Al^{3+}-doped polycrystalline films translate to enhanced optoelectronic properties. To understand the influence of Al^{3+} doping upon the photo-physical properties of the perovskite films we performed absorption and photoluminescence measurements, which we show in fig. S5. We observe little change in the absorption spectra for the films, but we do observe an increase in steady-state photoluminescence (PL) intensity with a maximum for the 0.15 mol% Al^{3+}-doped samples, and a subsequent fall off of in intensity upon further increase in doping concentration. In fig. 3 we compare the PL properties of the control films and those doped with 0.15 mol% Al^{3+}. In fig. 3a and 3b we observe that the Al^{3+}-doped perovskite films have higher steady state PL intensity and an almost two-fold increase in PL life time compared to the control.
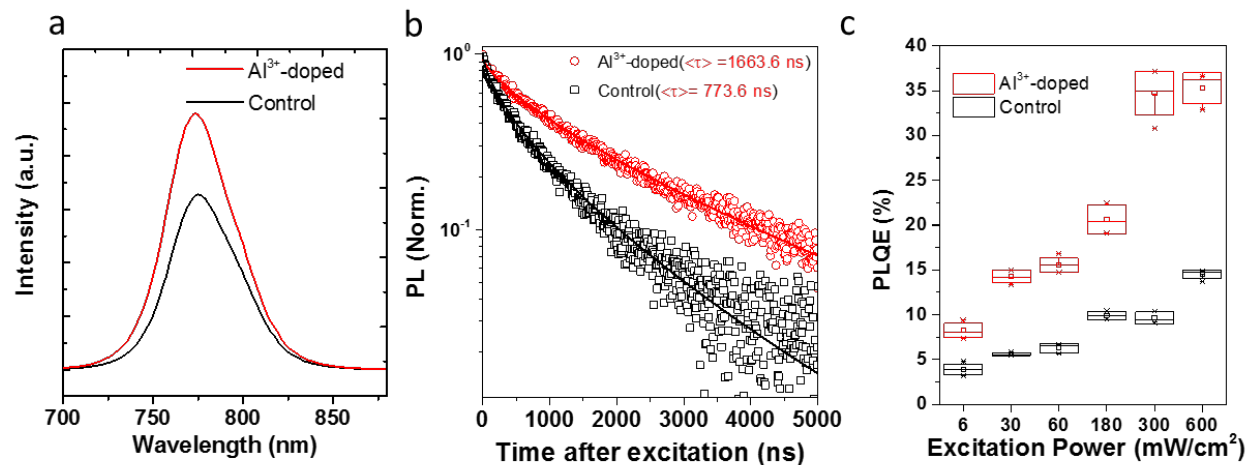
Figure 3: Photoluminescence spectroscopy of control (non-doped) and 0.15 mol% Al^{3+}-doped perovskite thin films deposited on glass substrate with **a**) steady-state spectra (300 mW/cm^2, 507 nm), **b**) time-resolved photoluminescence decay after excitation at 507 nm with pulsed (200 kHz) and a fluence of 30 nJ/cm^2/pulse, and **c**) photoluminescence quantum efficiency (PLQE) as a function of excitation power (further details are available in the supplementary materials).

To further quantify the influence of the Al^{3+} doping upon the radiative and non-radiative recombination rates, we performed photoluminescence quantum efficiency (PLQE) measurements as a function of excitation power, which we show in fig. 3c. For both doped and control samples, the PLQE rises with increasing excitation power, a behaviour attributed to the filling of trap states and increasingly favourable competition of radiative bimolecular recombination over non-radiative trap assisted recombination.[10,27,28] Notably, the PLQE is higher for the Al^{3+} doped samples at all light intensities, which, along with the increase we observe in the PL lifetime, is consistent with fewer fast non-radiative decay channels in the Al^{3+}-doped samples. We fit the bulk time-resolved PL data in fig. 3b with a stretched exponential function and extract the average lifetimes, <τ>, as previously described.[9] We use these low-fluence PL lifetime values along with the low excitation power (6 mW/cm^2) PLQE values, where in both

cases we expect the carrier recombination to be dominated by pseudo first-order kinetics,[9,28] to estimate the radiative and non-radiative decay rates in the films using,

$$PLQE = (\frac{k_{rad}}{k_{rad} + k_{non-rad}}), \qquad (3)$$

where k_{rad} is the radiative decay rate $k_{non-rad}$ is the non-radiative decay rate and $k_{rad} + k_{non-rad} = 1/<\tau>$. For the control and Al^{3+}-doped films, the k_{rad} we determine are similar for the two films at $5.04*10^4 \, s^{-1}$ and $4.96*10^4 \, s^{-1}$, while we observe a reduction in $k_{non-rad}$ from $1.24*10^6 \, s^{-1}$ to $5.52*10^5$ s^{-1} for the control and Al^{3+} doped films. This indicates that the substantive change in the photophysical properties of the perovskite films with 0.15 mol% Al^{3+} is approximately a two-fold reduction in the non-radiative recombination rate. We note that both the radiative and non-radiative decay rates are relatively low for a crystalline semiconductor. The slow recombination in metal halide perovskites is a highly fortuitous property for PV devices, but the origin of the phenomenon remains to be elucidated.[29]

The above analysis gives an indication of the macroscopic changes occurring within the perovskite films. However, we know that severe photophysical heterogeneity can occur within the polycrystalline films, and hence to clarify which microscopic regions of the film are responsible for the reduced non-radiative decay, we employ confocal fluorescence microscopy. In fig. 4a and b we show a 10 x 10 μm confocal fluorescence image of a control and 0.15 mol% Al^{3+}-doped perovskite film. We show the image histograms of occurrence versus PL (counts) in fig. 4c and d. In both films there exists heterogeneity in the PL emission with both bright and dark grains, and generally lower levels of PL in the regions near the grain boundaries. From the histograms it is apparent that the average number of PL counts (solid lines) of the Al^{3+} doped films have shifted to higher levels, but the distribution is similarly broad to that seen in the

control. In fact, the distribution has slightly broadened indicating no preferential spatial homogenisation of the PL, but simply an overall reduction in the non-radiative decay, both on or in the grains and at the grain boundaries. In Fig. S6, we performed Kelvin probe measurement in the dark and under illumination with perovskite films on FTO, and find a reduction in the surface photovoltage for Al^{3+}-doped films compared to control films, consistent with the removal of electronic traps in the former.

In order to quantify the electronic disorder in the films, we estimate the Urbach energy (E_u) of perovskite films from Fourier transform photocurrent spectroscopy, which we show in fig. S7. We estimate the E_u for the control and 0.15 mol% Al^{3+}-doped samples to be 13.09±0.05 and 12.64±0.04 meV respectively. This decrease in E_u is direct evidence for an enhancement of the electronic quality of the perovskite films by Al^{3+} doping. Notably, this is the first time an E_u has been determined to be less than 13 meV in a metal halide perovskite film, indicating the high electronic quality of the perovskite film[11,30], and suggesting an improved crystalline order in the polycrystalline thin film. The reason why the steepness of the absorption onset, and ultimately EQE spectra is important, is that this governs the maximum open-circuit voltage a solar cell can achieve in the "radiative limit", where all non-radiative recombination is switched off. We note that the first report of the E_u in perovskite films estimated a value of 15meV at room temperature. This is comparable to the E_u in crystalline silicon, but larger than the room temperature value in GaAs, which is as low as 7meV. However, the significant reduction to 12.6 meV so far, indicates that we have not yet reached the lower limit, and it may be possible that perovskites will end up closer to GaAs than crystalline silicon.
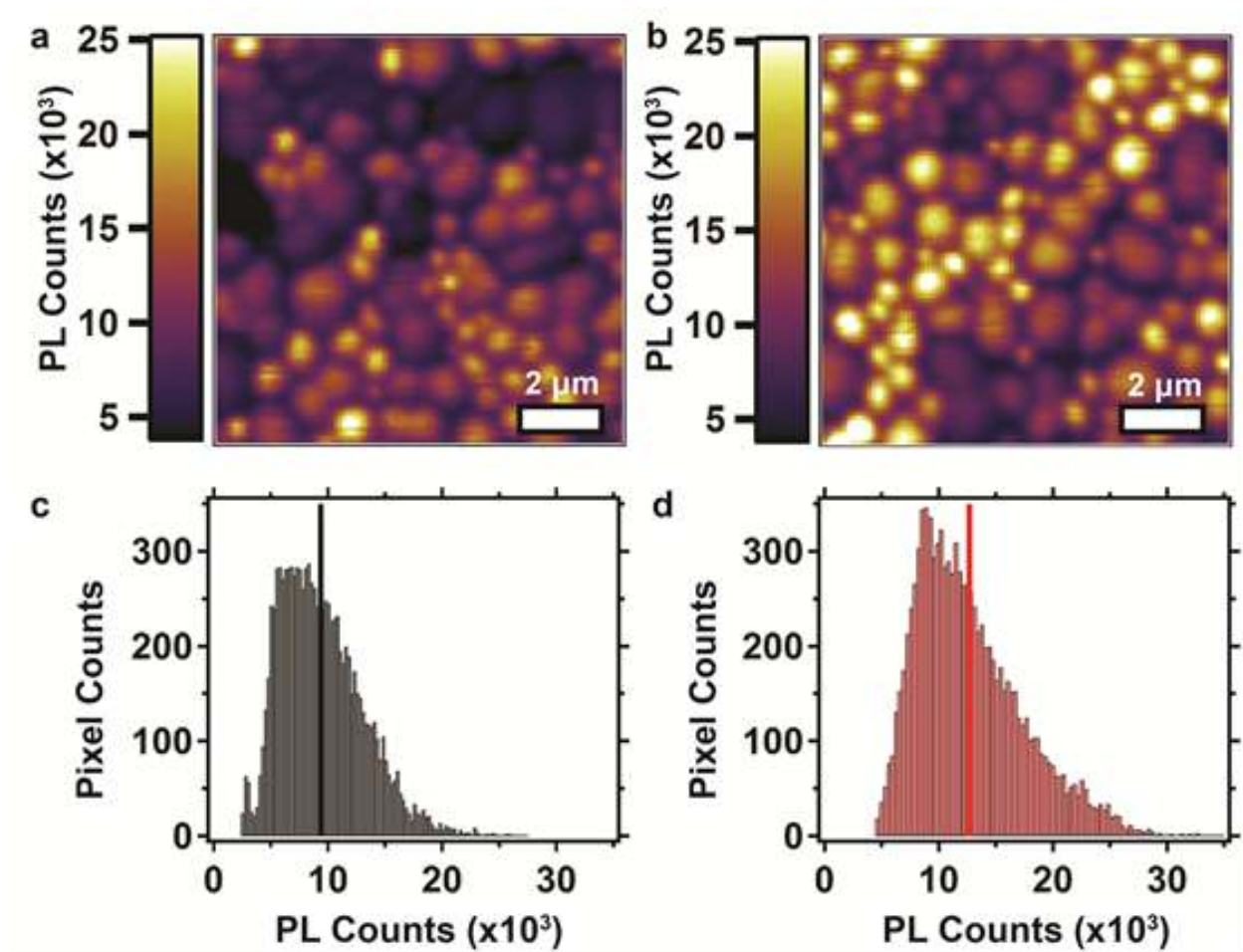
Figure 4: Fluorescence microscopy of (a) control and (b) Al^{3+}-doped (0.15 mol%) perovskite films with 10 x 10 μm area mapping excited with a pulsed 470 nm laser (40 MHz, 117 ps pulse width, 300 nJ/cm^2/pulse). (c) and (d) are the image histograms (10,000 pixels) showing the fluorescence emission distribution with solid lines indicate the average number of PL counts. The Al^{3+}-doped perovskite has more pixel counts falling under "bright" regions as compared to the control.

By interpreting the photo-physical and electronic impact of the Al^{3+} doping, it is apparent that the optimally doped films possess fewer non-radiative decay sites and are of superior electronic quality as compared with the control films. This is consistent with the enhanced structural quality we observed in fig. 1, resulting in improved optoelectronic performance. To assess if these enhanced film properties translate into enhancements in solar cell performance, we now integrate the perovskite films into "inverted" (p-i-n) planar heterojunction perovskite solar cells with a p-type organic hole transporting material (HTM), a solid "intrinsic" (i) perovskite film and an n-type organic electron transporting material.[31] We show a high angle annular dark field STEM (HAADF-STEM) cross-sectional micrograph of an optimized device in fig. 5a, an illustration of the energy levels of the materials employed in fig. 5b and a schematic of the full device architecture in fig. 5c. We note that the energy levels we illustrate are for the individual isolated materials, and upon doping and contact with each other there is likely to be a relative shift in the absolute energy at the interfaces.[32]
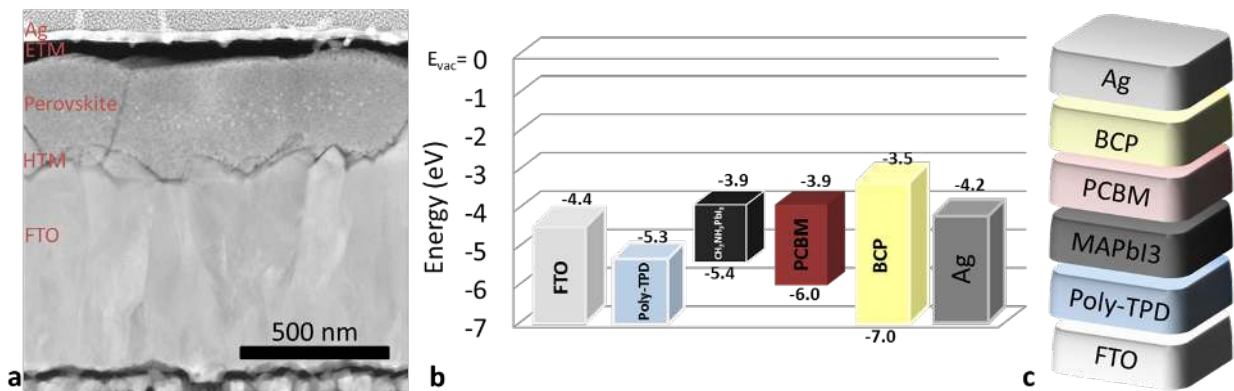

Figure 5: (a) High angle annular dark field STEM (HAADF-STEM) cross-sectional micrograph of optimized device with the structure of Ag/BCP/ETM (PCBM)/perovskite/HTM (poly-TPD)/FTO. **(b)** Diagram of the energy levels of the materials used and **(c)** an illustration of the structure of the solar cells.

In fig. S8 and in Table S1 we show the mean solar cell performance parameters for a batch of solar cells with a range of Al^{3+} doping concentrations, extracted from JV curves measured under simulated AM 1.5, 100 mW/cm^2 irradiance. We observe a clear trend of enhancement in device performance produced by the introduction of Al^{3+} dopant in to the perovskite precursor solution up to concentrations of around 0.15 to 0.3 mol%. For devices fabricated from the control precursor solution, i.e. pristine $MAPbI_3$, the average short-circuits current density (J_{sc}) and open circuit voltage (V_{oc}) are around 19.0±1.7mA/cm^2 and 1.01±0.04V, respectively. With the incorporation of the Al^{3+} dopant in the perovskite, both the J_{sc} and V_{oc} increase up to average values of 21.2±1.1 mA/cm^2 and 1.06±0.03 V, respectively, peaking at 0.15 mol%, while we observe that the average fill factor (FF) increases to 0.72±0.08with the addition of Al^{3+} up to 0.3 mol%, after which the FF begins to decrease. Hence, we observe the power conversion efficiency (PCE) to reach a maximum at 0.15 mol% of Al^{3+} doping, with an average PCE of the solar cells fabricated with this doping concentration of 15.8±2.4%. Notably, the optimized Al^{3+} doping not only improves all of the performance parameters (i.e. FF, V_{oc}, J_{sc} and PCE) as compared with the control devices, but also enhances device reproducibility, as we show in fig. S9.

In fig. 6a we show the current-density voltage (JV) curves for the most efficient control and Al^{3+} doped devices, where the latter exhibits a J_{sc} of 22.4 mA/cm^2, a FF of 0.78, and a V_{oc} of 1.10 V yielding a PCE of 19.1%. When we compare this with the control device, we can see that the major improvement is coming from the increases in V_{oc} and J_{sc}. The external quantum efficiency (EQE) spectra for typical cells of each type, which we show in fig. 6b, exhibit the same trend as the measured JV curves, consistent with the enhanced photocurrent from the Al^{3+} doped samples. Integrating the EQE over the AM1.5 solar spectrums at 100 mWcm^{-2} irradiance gives an

estimated J_{sc} of 20 and 18 mAcm^{-2} for the Al^{3+} doped and control devices, respectively. The measured J_{sc} under the solar simulator for these precise cells was 22.0 and 17.3 mAcm^{-2} respectively, which gives an indication of an accuracy of between -10 and + 4%, comparing the current estimated from the EQE to the JV measurements under simulated sun light. This difference may be within the measurement accuracy since we use two different rigs with two different calibration diodes. The cells are masked in the same manner for both measurements, however, the spatial uniformity of the EQE measurement is not as controlled as it is for the JV measurements, which may contribute to the errors. Additionally, we note that we test these cells in air without encapsulation, and there is usually a little degradation in performance for these p-i-n inverted cells following testing.

The JV curves for both control and Al^{3+}-doped perovskite solar cells exhibit very low levels of hysteresis. We illustrate this in fig. 6c showing the numerically averaged JV curves measured at different voltage sweep directions in a selection of 20 high performance devices with their performance parameters in the inset table. As an aside, this observation further strengthens our understanding that the main source of such hysteresis originates at the interface between the perovskite film and the semiconducting metal oxide such as TiO_2 or ZnO in regular device structures, probably due to the generation of a large density of electronic defects at the surface of the perovskite when the films are crystallised on these metal oxide surfaces.[33] Here, these cells using only organic p and n-type charge collection layers exhibit very well behaved current voltage characteristics. Notably, we have recently identified that the presence of electronic defects through which trap assisted recombination occurs, are central to the mechanism governing JV hysteresis in perovskite solar cells (combined with mobile ionic

species).[33] Our results are therefore consistent with the notion that perovskite films processed on organic semiconductors contain fewer electronic defects, than those processed on metal oxides.

Table 1. Best device performance parameters with different Al^{3+} doping concentration under simulated AM 1.5, 100 mW/cm^2 solar irradiation.

Al^{3+} doping concentration (mol%)	J_{sc} (mA/ cm^2)	V_{oc} (V)	FF (%)	PCE (%)
0	-21.3	-1.04	77.2	17.1
0.075	-21.1	-1.07	78.0	17.7
0.15	-22.4	-1.10	77.6	19.1
0.3	-21.8	-1.07	74.9	17.5
0.75	-20.3	-1.01	65.2	13.4
1.5	-9.9	-1.04	70.1	7.3

In fig. 6d, we show the stabilised power output (SPO) of the best performing control and Al^{3+} doped cells when holding the applied bias fixed at its maximum power point voltage under simulated AM 1.5 (100 mW/cm^2) sun light, and measuring the photocurrent as a function of time.

Both devices reach their stabilised photocurrent within the first measurement window, indicative of negligible hysteresis.[34] For the Al^{3+}-doped device, we measure a stabilized photocurrent at 20.3 mA/cm^2 and a stabilised power output (SPO) of 18.2 %, which is superior to the control device for which we measure a stabilized photocurrent and SPO of 18.2 mA/cm^2 and 15.7 %, respectively. We note that despite the negligible hysteresis in the JV curves, we still have slightly lower SPOs than the PCE determined from the JV curves. This emphasises that SPO measurements remain important even in cells appearing to exhibit negligible hysteresis. In fig. S10, we further show the average-SPO in a selection of 20 high performance devices at 17.7 % and 15.6 % for the Al^{3+}-doped and control devices respectively.
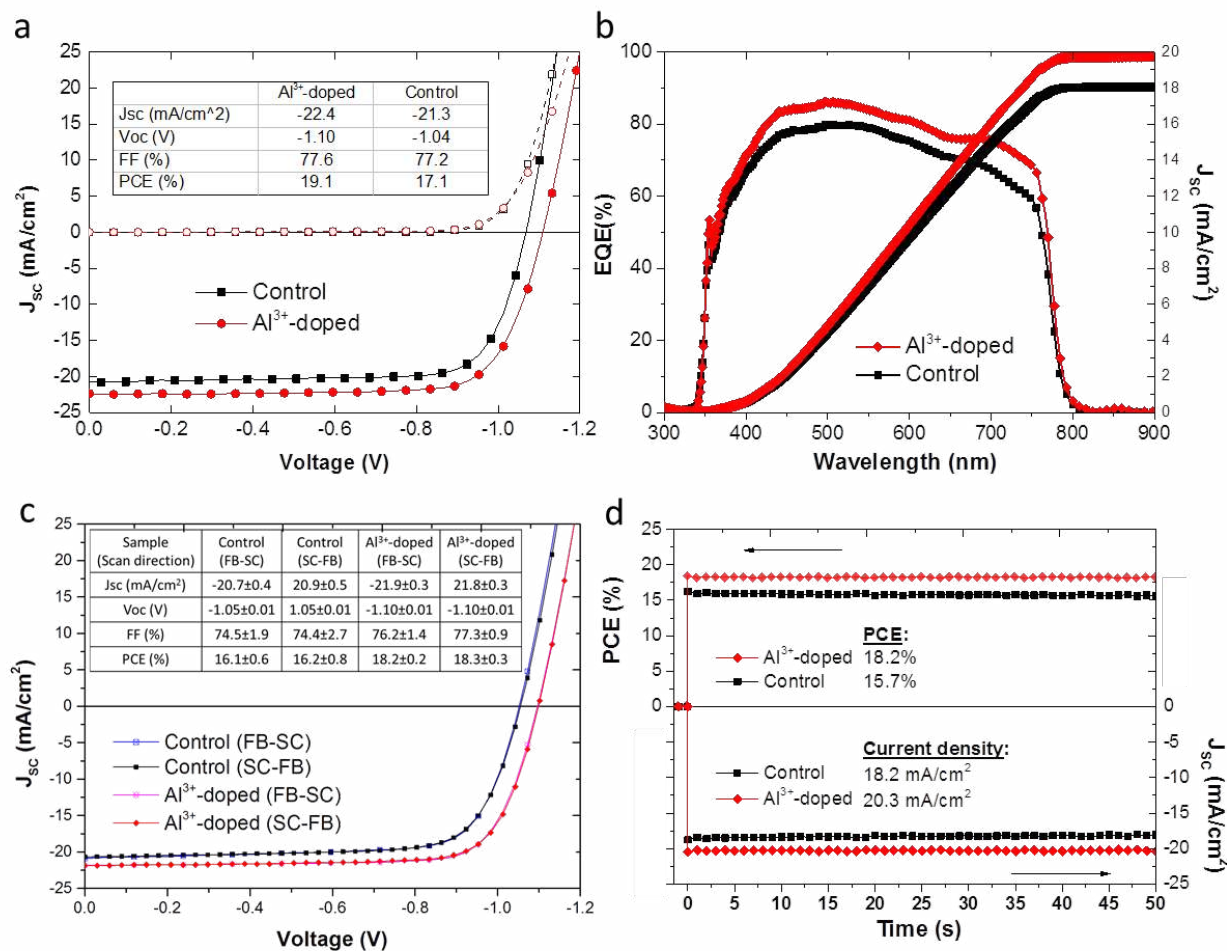
Figure 6: Photovoltaic performance of control and Al³⁺-doped (0.15 mol%) perovskite solar cells under simulated AM 1.5, 100 mW/cm² solar irradiation (solid line), and in the dark (dotted line) at a scan rate of 0.38 Vs⁻¹. **(a)** the current density-voltage characteristics of the best cells. **(b)** external quantum efficiency (EQE) spectrum measured at short-circuit, along with the expected photocurrent integrated over the AM1.5 solar spectrums of 100 mW/cm². **(c)** Numerically averaged *JV* curves measured from forward bias (FB) to short-circuit (SC) and back again without observable hysteresis in a selection of 20 high performance control and Al³⁺ doped devices. **(d)** Stabilized maximum power output measurement of the best cells with bias at their maximum power points.

To confirm that the positive effects we observe here are due to the addition of Al^{3+}, as opposed to the acac ion, we also replaced the $Al(acac)_3$ dopant with Aluminum iodide (AlI_3). These films exhibit enhanced luminescent properties, and subsequently deliver improved solar cells in comparison to the control devices. We show these results in fig. S11 where we observe that the addition of AlI_3 into perovskite precursor solution also delivers optimum performance with a doping level of around 0.15 mol%.

CONCLUSION

To summarize our findings, we have discovered that the electronic quality of the $MAPbI_3$ films can be substantially enhanced by low levels of doping with the small metal cation Al^{3+}. We have proposed the mechanism by which Al^{3+}-doping enhances the quality of the films, and revealed a simple property of the material, microstrain, which can be studied, tuned and minimised to deliver even higher quality perovskite films for optoelectronics. With the presence of Al^{3+} during the perovskite crystallization, we observe reduced microstrain in the perovskite crystal, which we infer to indicate a reduction in the density of crystal defects. From these same films we observe enhanced luminescent properties and reduced electronic disorder, which we infer to suggest that the same defects responsible for microstrain in the crystal, are also responsible for losses in luminescence and the solar cell operation. In addition, the remaining Al^{3+} ions present, most concentrated in the regions near the grain boundaries, may also act to alter the energy of these defect sites making them more benign. However, this latter consideration is not necessary to explain our results and is only a postulation. We have demonstrated improved JV measured PCE of up to 19.1% with negligible hysteresis for these Al^{3+}-doped films, when integrated into planar heterojunction solar cells. We attribute the improved operation to the reduced non-radiative trap assisted recombination in the thin films and

devices. Our work therefore highlights the possibility for considerable further improvement of the electronic quality of perovskite thin films, and subsequent devices by understanding the role of dopant impurities upon crystallisation, and crystal and electronic defects in perovskite thin films.

METHODS

Perovskite solution preparation

To form the control methylammonium lead iodide (MAPbI$_3$) precursor solution, it was prepared by mixing methylammonium iodide (Dyesol) and lead acetate trihydrate (Aldrich) at a 3:1 molar ratio, then dissolved in anhydrous N,N-Dimethylformamide with final concentrations of 30 wt% with the addition of hypophosphorous acid (3 ul/ml) as previously reported by Zhang et al.[11] For Al^{3+}-doped methylammonium lead iodide solution preparation, Aluminium acetylacetonate (Al-acac$_3$) was added into the MAPbI$_3$ precursor solution by desired Al^{3+}/Pb^{2+} ratios ranging from 0.075 to 1.5 mol%. (i.e. we add 3mg of Al-acac$_3$ into 1 g MAPbI$_3$ precursor solution to achieve the 1.5 mol% Al-acac$_3$ doping.)

Device fabrication

All the devices here were fabricated on piranha cleaned fluorine doped tin oxide (FTO) coated glass serving as the transparent electrode. We then deposit the hole-transporter material (HTM) of ~20 nm thickness by spin-coating a solution of F4-TCNQ-doped poly-TPD (1-Material Inc.) following the work of Wang et.al.[35] Then the perovskite layer was prepared by spin-coating at 2000 rpm for 45s from as-prepared precursor solution, drying the substrates for 10 min on the bench in the glovebox, followed by annealing at 100ºC for 5 min. For the n-type

collection layers, PCBM (dissolved in DCB, 2 wt%) was spin-coated on top of the perovskite films at 1000 rpm for 30s. Followed by the deposition of a thin (~5 nm) buffer layer of bathocuproine (BCP, 0.5 mg/ml in IPA) by spinning at 6000 rpm for 20 seconds. Finally, devices were completed by thermal evaporation of 70 nm of silver contacts under high vacuum.

ASSOCIATED CONTENT

Supplementary Information.

Full Experiment details, microstrain analysis, device characterization methods, device stability and reproducibility, FTPS, XPS, Photoluminescence, Kelvin probe measurement, NanoSIMS, UV-vis spectra on full series of Al^{3+}-doped perovskite.

REFERENCES

1   M. M. Lee, J. Teuscher, T. Miyasaka, T. N. Murakami and H. J. Snaith, *Science (80-.)*., 2012, **338**, 643–647.

2   M. Liu, M. B. Johnston and H. J. Snaith, *Nature*, 2013, **501**, 395–8.

3   J. H. Heo, S. H. Im, J. H. Noh, T. N. Mandal, C.-S. Lim, J. A. Chang, Y. H. Lee, H. Kim, A. Sarkar, M. K. Nazeeruddin, M. Grätzel and S. Il Seok, *Nat. Photonics*, 2013, **7**, 486–491.

4   N. J. Jeon, J. H. Noh, Y. C. Kim, W. S. Yang, S. Ryu and S. Il Seok, *Nat. Mater.*, 2014, **13**, 1–7.

5   M. Saliba, T. Matsui, J.-Y. Seo, K. Domanski, J.-P. Correa-Baena, M. K. Nazeeruddin, S. M. Zakeeruddin, W. Tress, A. Abate, A. Hagfeldt and M. Grä Tzel, *Energy Environ. Sci.*, 2016, **9**, -.

6 J. M. Ball, M. M. Lee, A. Hey and H. J. Snaith, *Energy Environ. Sci.*, 2013, **6**, 1739.

7 W.-J. Yin, T. Shi and Y. Yan, *Appl. Phys. Lett.*, 2014, **104**, 063903.

8 M. L. Agiorgousis, Y.-Y. Sun, H. Zeng and S. Zhang, *J. Am. Chem. Soc.*, 2014, **136**, 14570–5.

9 D. W. deQuilettes, S. M. Vorpahl, S. D. Stranks, H. Nagaoka, G. E. Eperon, M. E. Ziffer, H. J. Snaith and D. S. Ginger, *Science (80-.).*, 2015, **348**, 683–6.

10 N. K. Noel, A. Abate, S. D. Stranks, E. Parrott, V. Burlakov, A. Goriely and H. J. Snaith, *ACS Nano*, 2014, **8**, 140829182541001.

11 W. Zhang, S. Pathak, N. Sakai, T. Stergiopoulos, P. K. Nayak, N. K. Noel, A. A. Haghighirad, V. M. Burlakov, D. W. deQuilettes, A. Sadhanala, W. Li, L. Wang, D. S. Ginger, R. H. Friend and H. J. Snaith, *Nat. Commun.*, 2015, **6**, 10030.

12 J. Xu, A. Buin, A. H. Ip, W. Li, O. Voznyy, R. Comin, M. Yuan, S. Jeon, Z. Ning, J. J. McDowell, P. Kanjanaboos, J.-P. Sun, X. Lan, L. N. Quan, D. H. Kim, I. G. Hill, P. Maksymovych and E. H. Sargent, *Nat. Commun.*, 2015, **6**, 7081.

13 Y. Shao, Z. Xiao, C. Bi, Y. Yuan and J. Huang, *Nat. Commun.*, 2014, **5**, 5784.

14 W. Zhang, M. Saliba, D. T. Moore, S. K. Pathak, M. T. Hörantner, T. Stergiopoulos, S. D. Stranks, G. E. Eperon, J. A. Alexander-Webber, A. Abate, A. Sadhanala, S. Yao, Y. Chen, R. H. Friend, L. A. Estroff, U. Wiesner and H. J. Snaith, *Nat. Commun.*, 2015, **6**, 6142.

15 G. Kieslich, S. Sun and A. K. Cheetham, *Chem. Sci.*, 2014, **5**, 4712–4715.

16 I. Robinson and R. Harder, *Nat. Mater.*, 2009, **8**, 291–8.

17 A. Pramanick, X. P. Wang, C. Hoffmann, S. O. Diallo, M. R. V. Jørgensen and X.-L.

Wang, *Phys. Rev. B*, 2015, **92**, 174103.

18   G. . Williamson and W. . Hall, *Acta Metall.*, 1953, **1**, 22–31.

19   Y. Zhao and J. Zhang, *J. Appl. Crystallogr.*, 2008, **41**, 1095–1108.

20   D. T. Moore, H. Sai, K. W. Tan, D.-M. Smilgies, W. Zhang, H. J. Snaith, U. Wiesner and
         L. A. Estroff, *J. Am. Chem. Soc.*, 2015, **137**, 2350–8.

21   G. Kieslich, S. Sun and A. K. Cheetham, *Chem. Sci.*, 2015, **6**, 3430–3433.

22   R. A. Meyers, Ed., *Encyclopedia of Analytical Chemistry*, John Wiley & Sons, Ltd,
         Chichester, UK, 2006.

23   R. A. Berner, *Geochim. Cosmochim. Acta*, 1975, **39**, 489–504.

24   N. Kubota and J. W. Mullin, *J. Cryst. Growth*, 1995, **152**, 203–208.

25   K. Sangwal, *Prog. Cryst. Growth Charact. Mater.*, 1998, **36**, 163–248.

26   J. J. De Yoreo, P. U. P. A. Gilbert, N. A. J. M. Sommerdijk, R. L. Penn, S. Whitelam, D.
         Joester, H. Zhang, J. D. Rimer, A. Navrotsky, J. F. Banfield, A. F. Wallace, F. M. Michel,
         F. C. Meldrum, H. Colfen and P. M. Dove, *Science (80-.).*, 2015, **349**, aaa6760–aaa6760.

27   F. Deschler, M. Price, S. Pathak, L. E. Klintberg, D.-D. Jarausch, R. Higler, S. Hüttner, T.
         Leijtens, S. D. Stranks, H. J. Snaith, M. Atatüre, R. T. Phillips and R. H. Friend, *J. Phys.
         Chem. Lett.*, 2014, **5**, 1421–6.

28   S. D. Stranks, V. M. Burlakov, T. Leijtens, J. M. Ball, A. Goriely and H. J. Snaith, *Phys.
         Rev. Appl.*, 2014, **2**, 034007.

29   M. B. Johnston and L. M. Herz, *Acc. Chem. Res.*, 2015, **49**, 146–154.

30   S. De Wolf, J. Holovsky, S.-J. Moon, P. Löper, B. Niesen, M. Ledinsky, F.-J. Haug, J.-H. Yum and C. Ballif, *J. Phys. Chem. Lett.*, 2014, **5**, 1035–1039.

31   P. Docampo, J. M. Ball, M. Darwich, G. E. Eperon and H. J. Snaith, *Nat. Commun.*, 2013, **4**, 2761.

32   C.-C. Chueh, C.-Z. Li and A. K.-Y. Jen, *Energy Environ. Sci.*, 2015, **8**, 1160–1189.

33   S. van Reenen, M. Kemerink and H. J. Snaith, *J. Phys. Chem. Lett.*, 2015, **6**, 3808–3814.

34   H. J. Snaith, A. Abate, J. M. Ball, G. E. Eperon, T. Leijtens, N. K. Noel, S. D. Stranks, J. T.-W. W. Wang, K. Wojciechowski and W. Zhang, *J. Phys. Chem. Lett.*, 2014, **5**, 1511–1515.

35   Q. Wang, C. Bi and J. Huang, *Nano Energy*, 2015, **15**, 275–280.